

Enhancement in magnetic and electrical properties of Ni substituted Mg ferrite

K. RAMARAO¹, B. RAJESH BABU^{2,*}, B. KISHORE BABU³, V. VEERAI AH¹, K. RAJASEKHAR¹,
B. RANJITH KUMAR⁴, B. SWARNA LATHA¹

¹Department of Physics, Andhra University, Visakhapatnam, 530003, A.P., India

²Department of Physics, G.V.P. College of Engineering for Women, Visakhapatnam, 530048, A.P., India

³Department of Engineering Chemistry, AU College of Engineering, Visakhapatnam, 530003 A.P., India

⁴Advanced Functional Materials Research Centre, Department of Physics, KL University, Guntur, A.P., India

In this work, Ni substituted magnesium spinel ferrites having general formula $Mg_{1-x}Ni_xFe_2O_4$ (where $x = 0.0, 0.1, 0.15, 0.2, 0.25$ and 0.3) were synthesized by standard solid state reaction method. All the samples were characterized by X-ray diffraction (XRD), Fourier transform infrared spectroscopy (FT-IR), vibrating sample magnetometer (VSM), DC resistivity measurements. X-ray diffraction analysis confirmed the single spinel phase. The lattice constant decreased with increasing Ni content due to the difference in the ionic radii of Mg^{2+} and Ni^{2+} ions. The FT-IR spectra revealed two prominent frequency bands in the wave number range of 400 cm^{-1} to 600 cm^{-1} , which confirmed the cubic spinel structure of obtained compound and completion of chemical reaction. Magnetic studies revealed that the saturation magnetization increased with the substitution of Ni. The increase in magnetization was explained on the basis of distribution of magnetic and non-magnetic cations among A and B sites of the spinel lattice. A significant influence of cation distribution on DC electrical resistivity and activation energy was observed.

Keywords: *Mg-Ni ferrite; solid state reaction; XRD; VSM; FE-SEM*

1. Introduction

Spinel ferrites are promising ceramic magnetic materials and are a subject of intense theoretical and experimental investigations due to their remarkable electrical and magnetic properties. The spinel ferrites are widely used in the fields of magnetic resonance imaging (MRI), magnetic high-density information storage, etc. Among the spinel ferrites, Mg^{2+} and Ni^{2+} ferrites are soft magnetic n-type semiconducting materials, and are used in heterogeneous catalysis, adsorption, sensors, magnetic storage systems, magnetic resonance imaging, spintronics, LPG sensors, etc. [1].

A spinel unit cell is a face centered cubic structure, formed by 32 O^{2-} ions, which contains 64 tetrahedral (A) and 32 octahedral (B) interstitial sites. Among these, 8 tetrahedral A-sites and 16 octahedral B-sites are occupied by metal ions.

Therefore, substitution of different ions with different valence states in spinel ferrite, alters the cation distribution, which in turn, enhances or reduces its electromagnetic properties [2, 3].

Several authors reported the influence of various cations on Mg ferrites [4–8]. To the best of the authors' knowledge, there is no detailed report correlating structural modifications (microstructure) with the electromagnetic properties of Mg-Ni ferrites in the literature. Therefore, the present study is focused on the influence of Ni substitution in B-site and corresponding modifications in electrical and magnetic properties of $Mg_{1-x}Ni_xFe_2O_4$ (where $x = 0.0, 0.1, 0.15, 0.2, 0.25$ and 0.3) prepared by solid state reaction method.

2. Experimental

Samples of Ni substituted magnesium ferrite having various compositions $Mg_{1-x}Ni_xFe_2O_4$ with $x = 0.0, 0.1, 0.15, 0.2, 0.25, 0.3$ have been

*E-mail: rajeshbabu.bitra@gmail.com

synthesized by solid-state reaction method. High purity analytical grade (AR) precursors of MgO (99.9 % Himedia), Fe₂O₃ (99.9 % Himedia) and NiO (99.9 %) were used as starting materials in desired stoichiometric proportions. The starting precursors were weighed as per stoichiometric proportions and mixed thoroughly in an agate mortar with a pestle in acetone medium for 6 h. The mixed metal oxide powders were calcined at 900 °C for 4 h. The powders were compacted in the form of pellets by adding 5 % of polyvinyl alcohol (PVA) as a binder. Finally, the powder materials and pellets were sintered at 1200 °C for 4 h followed by natural cooling to room temperature.

3. Results and discussion

3.1. Structural analysis

3.1.1. Phase and lattice constant

X-ray diffraction patterns of all compositions of the system Mg_{1-x}Ni_xFe₂O₄ (x = 0.0, 0.1, 0.15, 0.2, 0.25 and 0.3) are shown in Fig. 1.

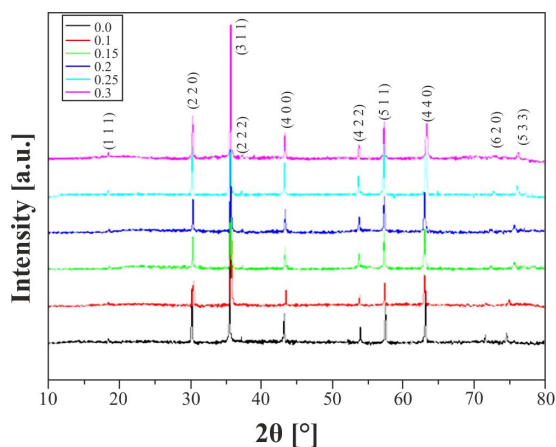


Fig. 1. XRD patterns of Mg_{1-x}Ni_xFe₂O₄ powders.

The reflections corresponding to the planes (1 1 1), (2 2 0), (3 1 1), (2 2 2), (4 4 0), (4 2 2) and (5 1 1) present in all samples provide the evidence of the formation of a spinel structure of the ferrite. These peaks correspond closely to the standard pattern of a spinel magnesium ferrite (ICSD# 01-073-1720) and no extra reflections are observed [9]. This confirms the formation

of a single-phase of the spinel compound without traces of any detectable impurities. The Rietveld refinement is a well-known and useful tool for structure determination [10]. It allows the determination of lattice parameters, atom positions, occupation parameters, isotropic and anisotropic temperature parameters. X-ray diffraction patterns were analyzed by general scattering analysis software (GSAS) using Rietveld refinement method. The Rietveld refinement of pure Mg ferrite is shown in Fig. 2.

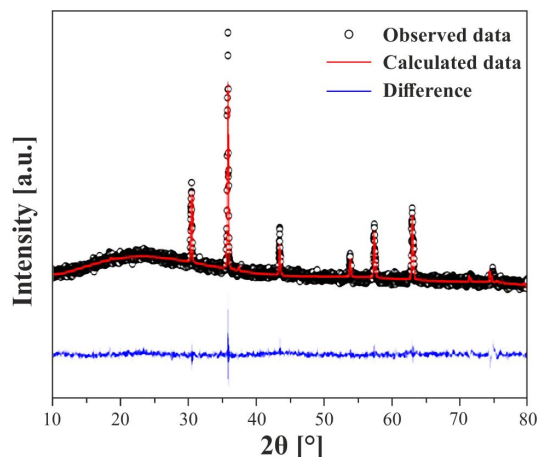


Fig. 2. Rietveld refined X-ray diffraction pattern of Mg_{1-x}Ni_xFe₂O₄ powder (x = 0).

The experimental lattice parameter a_{exp} was calculated according to the following equation:

$$a_{exp} = d\sqrt{h^2 + k^2 + l^2} \quad (1)$$

where d is the interplanar distance of each plane and $(h k l)$ are Miller indices. The calculated values of a_{exp} as a function of Ni content are shown in Fig. 3.

The lattice constant of undoped Mg ferrite is consistent with the values reported in the literature [11, 12]. In accordance to Vegard law, lattice constant continuously decreases as the substitution percentage of Ni²⁺ increases at the expense of Mg²⁺ ions. Similar behavior in the lattice constant as a function of Ni was reported in the literature [13]. The observed decrease in the lattice constant has been attributed to the difference

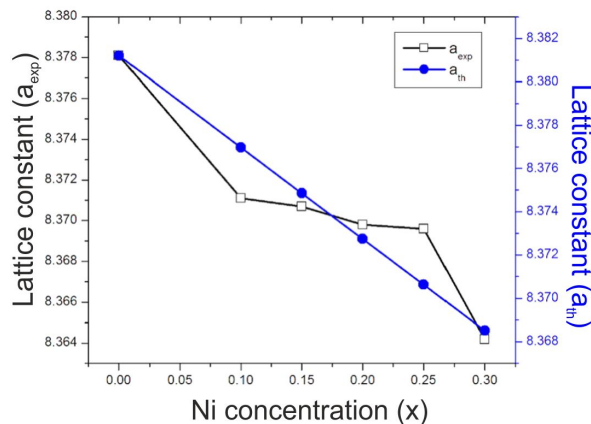


Fig. 3. Lattice parameter as a function of Ni concentration in $Mg_{1-x}Ni_xFe_2O_4$ powders.

in the radii of ions present in the sublattices. In the present work, Mg has a larger ionic radius than the other constituents (ionic radius of Mg^{2+} is 0.72 Å, Fe^{3+} is 0.60 Å and Ni^{2+} is 0.695 Å). The substitution of the smaller ionic radius Ni^{2+} (0.695 Å) ions in place of large Mg^{2+} (0.72 Å) ions and their occupancy ratio in tetrahedral and octahedral sites resulted in a gradual decrease in the value of lattice constant.

It is also observed (Fig. 3) that variation in the lattice constant is small with the substitution of Ni ions. This is due to the fact that a fraction of larger Mg^{2+} ions occupies tetrahedral A sites, which displace Fe^{3+} ions in octahedral sites. This causes a small variation in the lattice constant. The average crystallite size D_{311} , cell volume V_c , X-ray density d_x were calculated from XRD data, while the bulk density was measured by considering mass to volume ratio and the results are listed in Table 1. Crystallite size D was calculated by the following well-known Scherrer equation:

$$D_{311} = \frac{k\lambda}{\beta \cos\theta} \quad (2)$$

where k is the Scherrer constant, λ is the wavelength of X-ray used, β is the full width at half maximum, θ is the Bragg angle:

$$V_c = a_{exp}^3 \quad (3)$$

$$d_x = \frac{ZM_w}{N_A V_c} \quad (4)$$

where Z is the number of formula units in a unit cell, M_w is the molecular weight of the sample, N_A is the Avogadro number and V_c volume of the cell.

The average crystallite size in the Ni substituted samples was found to be in the range of 41 nm to 47 nm (Table 1). No significant change in crystallite size has been observed with Ni^{2+} substitution. It is clear from Table 1 that the cell volume V_c also follows the trend similar to the lattice constant due to lattice shrinkage (Table 1). On the contrary, the value of the X-ray density, d_x increases with the increase in Ni^{2+} content (Table 1) due to larger molar mass of substituted Ni, when compared with Mg. In general, the magnitude of the bulk density d_b , is smaller than the one of the X-ray density d_x due to the presence of pores created during the sintering process. The decrease in density can be ascribed to the difference in the atomic weight and density of Mg^{2+} (24.31 g/cm³ and 1.74 g/cm³, respectively), which are lower than those of Ni^{2+} (58.69 g/cm³ and 8.90 g/cm³).

3.1.2. Cation distribution and theoretical lattice constant

In order to understand the variation in lattice parameter, the distribution of cations among tetrahedral A and octahedral B sites was estimated using a well-known X-ray intensity calculation method reported by Burger [14]. This method is quite suitable if there exists a significant difference in scattering factors of the ions (Ni^{2+} and Mg^{2+}). The investigation of cation distribution provides a mean to develop materials with desired properties which are useful for many devices [15]. The XRD intensities of various Bragg planes, such as (2 2 0), (3 1 1), (4 0 0), (4 4 0) and (4 2 2), have been considered, as the intensities of these planes are the most sensitive to the cation distribution in A and B sites:

$$I_{hkl} = |F_{hkl}|^2 P_m \cdot L_p \quad (5)$$

where I_{hkl} is the relative integrated intensity, F_{hkl} is the structure factor, P_m is the multiplicity factor and L_p is the Lorentz polarization factor. In the process of arriving at the final cation distribution, the site occupancy of all the cations was varied in many combinations and those that agreed well with

Table 1. Average crystallite size D_{311} , volume of the cell V_c , density – d_b , d_x – and porosity P of $Mg_{1-x}Ni_xFe_2O_4$ with composition x .

Composition x	Average crystallite size [nm]	Bulk density [g/cm^3]	X-ray density [g/cm^3]	Volume of the cell [\AA^3]	Porosity P [%]
0.0	47.1	4.24	4.53	588.08	6.4
0.1	46.38	4.14	4.61	586.61	10.1
0.15	46.66	4.17	4.65	586.52	10.16
0.2	41.49	4.11	4.68	586.33	12.19
0.25	45.23	4.15	4.73	586.29	12.12
0.3	44.59	4.18	4.77	585.15	12.42

the experimental intensity of the diffracted beam were taken into consideration. The final cation distribution, obtained for $Mg_{1-x}Ni_xFe_2O_4$ system is given in Table 2. It is clear that Mg^{2+} ions occupy both A and B sites simultaneously, but with different ratios. The occupation of Mg^{2+} ions in B-site results in migration of a fraction of Fe^{3+} ions into A-sites. As mentioned before, this kind of modification in the cation distribution alters the electromagnetic properties of the ferrite.

Using the cation distribution, lattice parameter has been calculated theoretically from the following relation, since there is a correlation between the ionic radii of both A and B-sublattices and the lattice parameter:

$$a_t = \frac{8}{3\sqrt{3}} \left[(r_A + r_o) + \sqrt{3}(r_B + r_o) \right] \quad (6)$$

where r_o is the radius of the oxygen ion (0.132 nm) and r_A and r_B are the ionic radii of tetrahedral A-site and octahedral B-site, respectively. The values of the theoretical and experimental lattice parameters follow the same trend for all values of x , which confirms the correctness of the suggested cation distribution.

3.1.3. Infrared spectra

Infrared spectroscopy is an important tool to identify the functional groups, phase and purity of samples. Fig. 4 depicts the FT-IR spectra of Ni^{2+} substituted $MgFe_2O_4$ in the range of 1000 cm^{-1} to 400 cm^{-1} . It is observed that the two metal oxides reveal broad and narrow absorption bands (ν_1 and ν_2) corresponding to the metal-oxide (M–O)

stretching vibrations of tetrahedral ν_1 and octahedral ν_2 sites around 570 cm^{-1} and 400 cm^{-1} , respectively. Therefore, it provides a supportive evidence for XRD result with respect to the formation of single cubic spinel phases. The difference in the frequency assignment is due to the difference in the bond length between octahedral and tetrahedral coordinates. In the spectra shown in Fig. 4, a small shifting of frequency in both tetrahedral and octahedral bands with increasing Ni^{2+} concentration is noticeable. The tetrahedral bands are shifted from lower band value (572.88 cm^{-1}) to higher band value (582.52 cm^{-1}). The octahedral bands are shifted from higher band value (410 cm^{-1}) to lower band value (401.02 cm^{-1}).

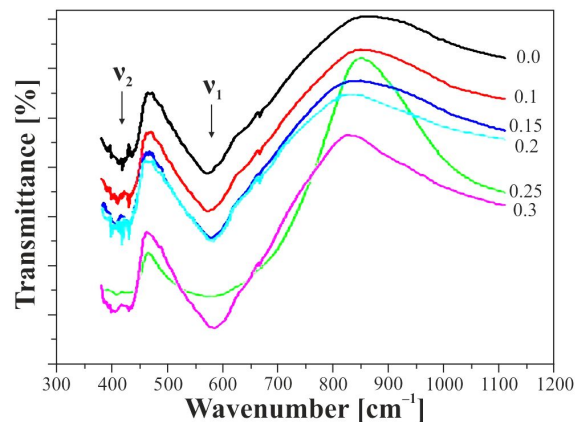


Fig. 4. Infrared spectra of $Mg_{1-x}Ni_xFe_2O_4$ powders as a function of Ni concentration.

The shifting of ν_1 and ν_2 confirms the cation distribution in both octahedral and tetrahedral sites. In general, the shift towards higher frequency can

Table 2. Cation distribution of $\text{Mg}_{1-x}\text{Ni}_x\text{Fe}_2\text{O}_4$ with composition x .

Composition x	I_{220}/I_{400}	I_{400}/I_{422}	I_{220}/I_{400}	I_{400}/I_{422}	A-site	B-site
	calc.		exp.			
0.0	1.1232	0.9032	1.1911	0.8612	$\text{Mg}_{0.2}^{2+}\text{Fe}_{0.8}^{3+}$	$\text{sMg}_{0.8}^{2+}\text{Fe}_{1.2}^{3+}$
0.1	0.8601	1.1191	0.7963	0.9551	$\text{Mg}_{0.09}^{+2}\text{Fe}_{0.91}^{+3}$	$\text{Ni}_{0.1}^{+2}\text{Mg}_{0.81}^{+2}\text{Fe}_{1.09}^{+3}$
0.15	0.8576	1.1226	0.6474	1.1731	$\text{Mg}_{0.085}^{+2}\text{Fe}_{0.915}^{+3}$	$\text{Ni}_{0.15}^{+2}\text{Mg}_{0.765}^{+2}\text{Fe}_{1.085}^{+3}$
0.2	0.8584	1.1218	0.7146	1.0645	$\text{Mg}_{0.08}^{+2}\text{Fe}_{0.92}^{+3}$	$\text{Ni}_{0.2}^{+2}\text{Mg}_{0.72}^{+2}\text{Fe}_{1.08}^{+3}$
0.25	0.8592	1.1211	0.6735	1.0987	$\text{Mg}_{0.075}^{+2}\text{Fe}_{0.925}^{+3}$	$\text{Ni}_{0.25}^{+2}\text{Mg}_{0.675}^{+2}\text{Fe}_{1.075}^{+3}$
0.3	0.8608	1.117	0.6735	1.0987	$\text{Mg}_{0.07}^{+2}\text{Fe}_{0.93}^{+3}$	$\text{Ni}_{0.3}^{+2}\text{Mg}_{0.63}^{+2}\text{Fe}_{1.07}^{+3}$

be attributed to the shifting of Fe^{+3} ions towards the O^{-2} ions [16]. The band frequencies ν_1 and ν_2 , are reported in Table 3.

Besides, the octahedral bands exhibit splitting of absorption bands including few small subsidiary bands. Detected subsidiary bands are mainly due to John-Teller distortion evolved by the presence of ferrous Fe^{2+} ions [17]. The force constant can be calculated for tetrahedral site K_t and octahedral site K_o using the method suggested by Waldron [18]:

$$K_t = 7.62 \times M_1 \times \vartheta_1^2 \times 10^{-7} N/m \quad (7)$$

$$K_o = 10.62 \times \frac{M_2}{2} \times \vartheta_2^2 \times 10^7 N/m \quad (8)$$

where M_1 and M_2 are the molecular weights of cations at A and B-sites, respectively. Both M_1 and M_2 were calculated from the cation distribution data presented in Table 2. The calculated values of the force constants K_t and K_o are listed in Table 3. It can be seen that both K_t and K_o increase with increasing Ni^{2+} content. Furthermore, the fact that the calculated values of K_t are greater than those of K_o is due to the difference in bond length of A-site r_A that are smaller than those of B-site r_B . The increase in force constants with increasing Ni^{2+} content suggests the strengthening of interatomic bonding.

3.1.4. Scanning electron microscopic study

It is well known that a shape and size of a grain is strongly influenced by the electrical and magnetic properties of the ferrite. The surface

morphology of the samples was determined by the field emission scanning electron microscope (FE-SEM). The images of the Ni^{2+} substituted $\text{Mg}_{1-x}\text{Ni}_x\text{Fe}_{2-x}\text{O}_4$ (where $x = 0.0, 0.1, 0.15, 0.2, 0.25$ and 0.3) are shown in Fig. 5. The micrographs clearly show the presence of larger grains, which are well crystallized with uneven size, and have less agglomerations due to the relatively higher sintering temperature. The values of average grain size for each sample were estimated using Image J4 Software and are presented in Table 3. The average grain size decreases linearly with increasing Ni^{2+} content.

3.1.5. Interionic bonds

The changes in the bond lengths and bond angles between the cation-cation (Me–Me) and cation-anion (Me–O) alters the overall strength of the magnetic interactions (A–A, B–B and A–B) in A and B sublattices. The bond angles ($\theta_1, \theta_2, \theta_3, \theta_4$ and θ_5) have been calculated by simple trigonometric principle using the interionic distances with the help of the formulae listed in Table 4. It is well known that bond lengths and bond angles between cations and cation-anion are likely to influence the magnetic interaction between the sublattices. The strength of the magnetic interaction is inversely related to the bond length and directly related to the bond angle. In spinel ferrite, magnetic moments of A and B sites are aligned in a direction opposite to each other. Thus, the resultant magnetic moment depends on the difference in the magnetic moments of A and B sites. The magnetic interaction between ions present at A and B

Table 3. Positions of IR bands ν_1 and ν_2 , force constants K_t and K_o and average grain size of $Mg_{1-x}Ni_xFe_2O_4$ with composition x .

Composition x	ν_1 [cm^{-1}]	ν_2 [cm^{-1}]	K_t [N/m]	K_o [N/m]	average grain size [μm]
0.0	572.88	410	132	74.4	1.22
0.1	574.81	407.96	128	76.4	0.9987
0.15	576.74	408.92	130	78.1	0.971
0.2	579.63	406.03	132	78.4	0.8949
0.25	579.63	402	132	78.2	0.8742
0.3	582.52	401	134	79.1	0.8284

sites is comparatively stronger than the interaction of ions in the same sublattice, i.e. A-A or B-B. The substitution of magnetic or non-magnetic ions in the spinel ferrite alters the cation distribution. If the substituted ion has a different ionic radius, it causes an increase/decrease in the bond length and bond angle.

This may enhance or reduce the magnetic interaction and affects the magnetic properties of the ferrite. The estimated bond lengths shown in Table 5 reveal that interionic distances between cations at (A-A), (B-B) and (A-B) and cation-anion (A-O, B-O) change with increasing Ni content. The increasing trend observed in bond angles $\theta_{(1)}$ and $\theta_{(2)}$ (Table 5) suggests the strengthening of A-B interactions, while $\theta_{(3)}$, $\theta_{(4)}$ and $\theta_{(5)}$ are found to be not changed with increasing Ni^{2+} concentration. However, deviation from linear increase/decrease in the values is due to the difference in the occupancy ratios of cations among tetrahedral (A) and octahedral (B) sites.

3.2. Saturation magnetization and coercivity

Fig. 6 shows the magnetization measurement results of Ni^{2+} substituted Mg ferrite samples measured at room temperature and corresponding hysteresis loops. The magnetization of the undoped Mg ferrite sample increases with the strength of applied field and the magnetization of material attains maximum of 20.36 emu/g at the applied field strength of 19 kOe.

The lower value of magnetization for undoped Mg ferrite is caused by occupation of larger

concentration of non-magnetic magnesium cations at B-site. The obtained magnetization value of the pristine Mg ferrite is comparatively less than the reported values [19, 20]. The saturation magnetization and coercivity obtained from hysteresis loops are listed in Table 6.

The observed increase in magnetization with increasing Ni^{2+} concentration can be explained based on Neel two sublattice model. According to the Neel two sublattices model, metal ions are distributed in two crystallographic sites, namely tetrahedral A and octahedral B. The magnetic moments of A and B sites are aligned in opposite directions. Thus, the net magnetic moment is the difference between the magnetic moments of A and B sites, i.e. $M = |M_B - M_A|$. It is reported in the literature that magnesium ferrite and nickel ferrite exhibit inverse spinel structure at room temperature [20].

In the present study, the magnetic Ni^{2+} ($2\mu_B$) ions replace non-magnetic Mg^{2+} ($0\mu_B$) ions. Therefore, one can expect an increase in magnetization with increasing Ni content. In general, Mg^{2+} and Fe^{3+} ions are partially distributed in A and B sites in different proportions. The Ni^{2+} ions occupy octahedral sites B, which displaces a fraction of Fe^{3+} ions into octahedral A sites. This causes an increase in the magnetic moment of A site and B sites. Thus, the resultant magnetic moment of the spinel lattice increases. The present cation distribution estimated from X-ray line intensity calculations (Table 2) supports the observed variation in magnetization. This suggests that the present distribution is more or less equal to the original distribution. Coercivity is the minimum reverse

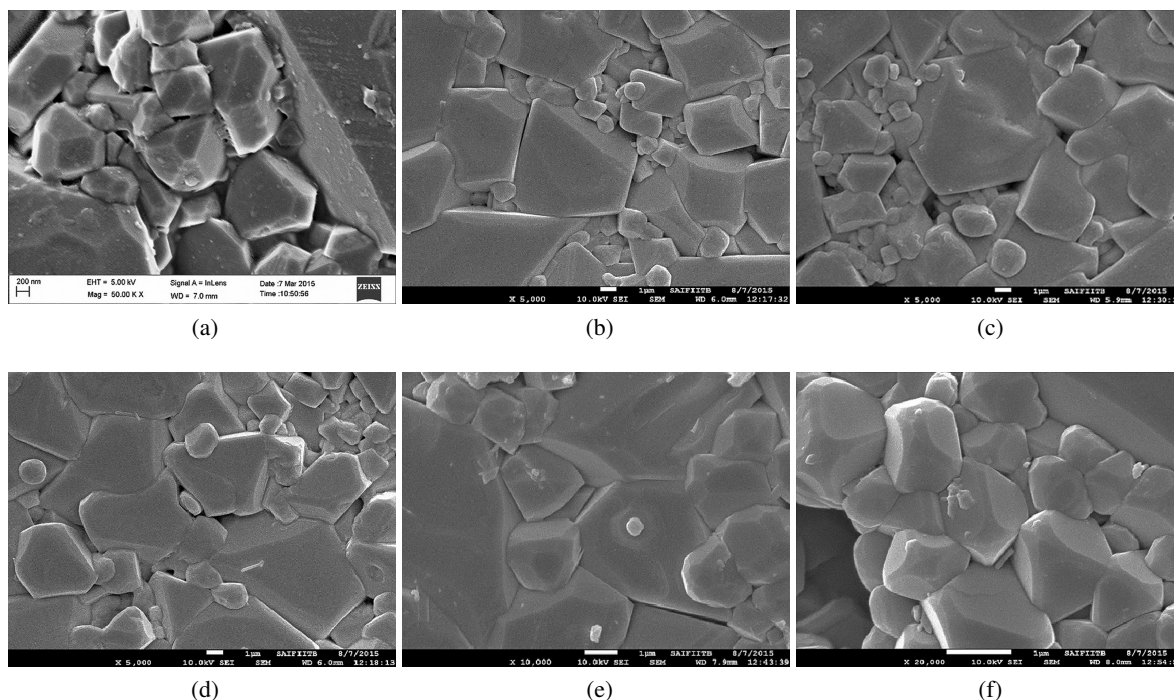


Fig. 5. FE-SEM images of $\text{Mg}_{1-x}\text{Ni}_x\text{Fe}_2\text{O}_4$ powders (a) $x = 0.0$, (b) $x = 0.1$, (c) $x = 0.15$ (d) $x = 0.2$ (e) $x = 0.25$ and (f) $x = 0.3$.

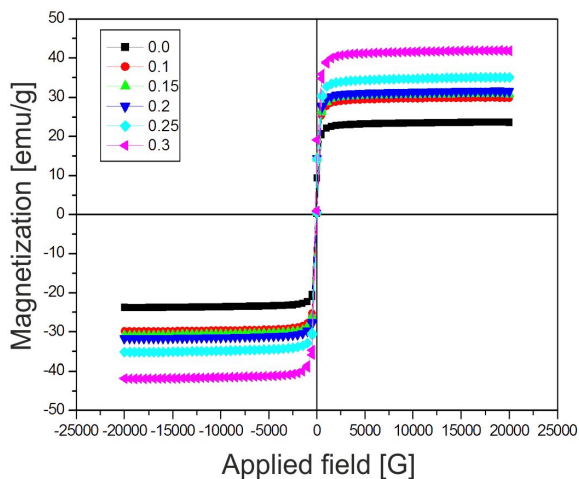


Fig. 6. Hysteresis loops of $\text{Mg}_{1-x}\text{Ni}_x\text{Fe}_2\text{O}_4$ powders.

magnetic field strength required to reduce remanence to zero. Coercivity in a ferrite system is known to depend on various parameters, like magnetocrystalline anisotropy, lattice imperfections, dislocations, internal strains, grain size and shape, porosity and secondary phases. In the present

investigation, decrease in grain size and non-uniform distribution of Fe^{3+} ions (changes in anisotropy of the spinel unit cell) might be responsible for the observed variation in coercivity.

3.3. DC electrical resistivity

The temperature dependence of electrical resistivity ρ of $\text{Mg}_{1-x}\text{Ni}_x\text{Fe}_2\text{O}_4$ is shown in Fig. 7. It is clear that all the samples exhibit a linear relationship with temperature. This confirms the semiconducting nature of the prepared samples. It has been observed from Fig. 8 that resistivity increases with increasing Ni^{2+} concentration. This change in resistivity can be explained based on the hopping mechanism. The spinel ferrites are known to be low-mobility materials and their conductivity is governed by the charge carrier transfer between similar ions (with different valence states) present at different octahedral sites, through a process known as “hopping mechanism” [21]. Thus, hopping of electron between Fe^{2+} and Fe^{3+} ions located at octahedral sites is the primary mechanism which allows electrical transport.

Table 4. Interionic bond lengths and angles in spinel ferrites.

Interaction between sublattices	Interionic	
	Distance [Å]	Bond angles [°]
A-A	$d = \left(\frac{a}{4}\right) \sqrt{3}$	$\theta_{(5)} = \cos^{-1} \left[\frac{r^2 + q^2 - d^2}{2rq} \right]$
B-B	$b = \left(\frac{a}{4}\right) \sqrt{2}$	$\theta_{(3)} = \cos^{-1} \left[\frac{2p^2 - b^2}{2p^2} \right]$
	$f = \left(\frac{a}{4}\right) \sqrt{6}$	$\theta_{(4)} = \cos^{-1} \left[\frac{p^2 + s^2 - f^2}{2ps} \right]$
A-B	$c = \left(\frac{a}{8}\right) \sqrt{11}$	$\theta_{(2)} = \cos^{-1} \left[\frac{p^2 + r^2 - e^2}{2pr} \right]$
	$e = \left(\frac{3a}{8}\right) \sqrt{3}$	$\theta_{(1)} = \cos^{-1} \left[\frac{p^2 + q^2 - c^2}{2pq} \right]$
A-O	$q = a \left(u^{3m} - \frac{1}{8} \right) \sqrt{3}$	
	$r = a \left(u^{3m} - \frac{1}{8} \right) \sqrt{11}$	
B-O	$p = a \left(\frac{1}{2} - u^{3m} \right)$	
	$s = \frac{a}{3} \left(u^{3m} + \frac{1}{2} \right) \sqrt{3}$	

When the samples are sintered at high temperature, the formation of oxygen vacancies causes conversion of some Fe^{3+} ions into Fe^{2+} ions to maintain charge neutrality of the spinel lattice. It has been reported that presence of 0.3 % Fe^{2+} content in a ferrite can reduce the electrical resistivity by a factor of more than two orders of magnitude [22]. It was reported that the Ni^{2+} ion of resistivity $6.99 \times 10^{-6} \Omega\cdot\text{cm}$ has a strong preference to occupy octahedral B sites whereas the Mg^{2+} ion of resistivity $4.29 \times 10^{-6} \Omega\cdot\text{cm}$ and the Fe ion of resistivity $9.9 \times 10^{-6} \Omega\cdot\text{cm}$ tend to occupy B

and A sites [23]. When Ni^{2+} ion addition of higher resistivity increases at the B sites, replacing Mg^{2+} ions of lower resistivity, some Mg^{2+} and Fe ions will migrate from B sites to A sites. This, in turn, reduces the availability of Fe^{3+} ions at B sites, and thereby, increases the resistivity.

The electrical resistivity of ferrites also depends upon the activation energy, which is associated with the electrical energy barrier experienced by the electrons during hopping. The values of activation energy were calculated using the following

Table 5. Interionic bond lengths and angles in $\text{Mg}_{1-x}\text{Ni}_x\text{Fe}_2\text{O}_4$ with composition x .

Composition x	0.0	0.1	0.15	0.2	0.25	0.3
u(3m)	0.2317	0.2318	0.2318	0.2318	0.2318	0.2318
u(43m)	0.3792	0.3792	0.3792	0.3792	0.3792	0.3792
b	2.9621	2.9596	2.9595	2.9592	2.9591	2.9572
c	3.4734	3.4705	3.4703	3.4699	3.4699	3.4676
d	3.6278	3.6248	3.6246	3.6242	3.6241	3.6218
e	5.4417	5.4372	5.4369	5.4363	5.4362	5.4327
f	5.1305	5.1262	5.126	5.1254	5.1253	5.122
p	2.2475	2.2454	2.2451	2.2448	2.2446	2.243
q	1.549	1.5481	1.5482	1.5483	1.5485	1.5477
r	2.966	2.9644	2.9646	2.9647	2.9651	2.9636
s	3.5395	3.5367	3.5366	3.5363	3.5363	3.5341
$\theta(1)$	131.57	131.56	131.55	131.55	131.54	131.54
$\theta(2)$	143.77	144.33	144.9	145.01	146.45	146.92
$\theta(3)$	82.49	82.5	82.5	82.51	82.51	82.52
$\theta(4)$	123.4	123.4	123.4	123.4	123.4	123.41
$\theta(5)$	102.4	102.35	102.33	102.3	102.28	102.26

Table 6. Magnetization and coercivity of $\text{Mg}_{1-x}\text{Ni}_x\text{Fe}_2\text{O}_4$ with composition x .

Parameters	$x = 0.0$	$x = 0.1$	$x = 0.15$	$x = 0.2$	$x = 0.25$	$x = 0.3$
Magnetization M_s [emu/g]	20.36	29.85	31.03	32	35	42
Coercivity H_c [G]	157	266	173	256	159	193

relation and are shown in Fig. 8 as a function of Ni concentration. The relationship between resistivity and temperature may be expressed as:

$$\rho_{(T)} = \rho_o \cdot e^{\frac{\Delta E}{k_B T}} \quad (9)$$

where ρ_o is the pre-exponential factor with dimension of $\Omega\text{-cm}$, $\rho_{(T)}$ is the resistivity at T , ΔE is the activation energy for conduction, K_B is the Boltzmann constant and T [K] is the absolute temperature. The activation energy ΔE of the studied specimens was found within the range of 0.32 to 0.42, which is in good agreement with previously reported values for other spinel ferrites [24]. It is well known that grain size, density and porosity strongly influence the conductivity of ferrites [25]. Fig. 8 clearly shows that grain size and activation energy follow the inverse trend with each other. As discussed above, hopping decreases with decreasing grain size. This is due to the fact that grain

boundaries act as poor conductors. With decreasing grain size, no grain boundaries increase and reduce the hopping of charge carriers. In addition to that, an increase in porosity is also responsible for the enhancement in the resistivity.

4. Conclusions

The results of this work could be summarized as follows: the presence of Ni ions in $\text{Mg}_{1-x}\text{Ni}_x\text{Fe}_2\text{O}_4$ causes changes in the structural, magnetic and electrical properties of this compound. The formation of cubic spinel phase was confirmed by X-ray diffraction and IR spectra. Structural, electrical and magnetic properties were analyzed as a function of Ni concentration. Lattice parameter decreases with increasing Ni substitution but the variation is small. Saturation magnetization follows a linear trend.

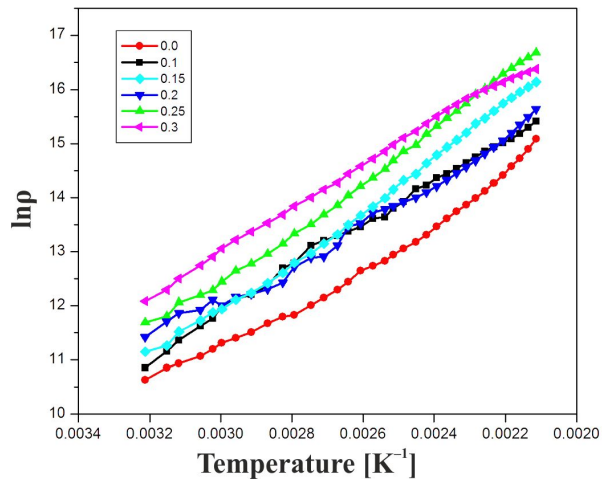


Fig. 7. Temperature dependence of DC electrical resistivity of $Mg_{1-x}Ni_xFe_2O_4$ powders.

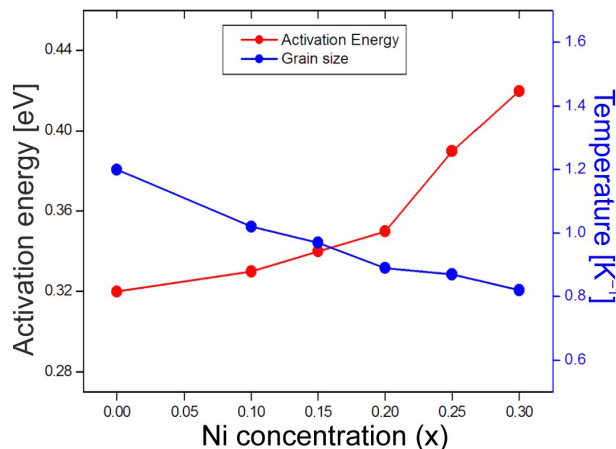


Fig. 8. Activation energy and grain size as a function of Ni content.

DC resistivity and activation energy increase, as the presence of Ni^{2+} ions at B sites reduces the conduction of charge carriers. It is observed that a control over grain size and cation distribution is important to enhance the electric and magnetic properties. We have also examined the influence of divalent ion substitution like Co^{2+} [26] and Zn^{2+} [27] in $MgFe_2O_4$. It is observed that Ni^{2+} substitution enhances the magnetic and electrical properties when compared with Co^{2+} and Zn^{2+} substitution. This might be attributed to the occupancy of Ni^{2+} at B site and reduction of grain size. Another important factor for increasing the resistivity is due to

the reduction of possible formation of Fe^{2+} ions at B-sites, which further hinders the hopping process.

Acknowledgements

One of the authors, Mr.K. Rama Rao, is thankful to UGC for providing BSR (SAP) scholarship and B. Kishore Babu and K. Mohana Rao are grateful to UGC for their financial assistance the file name of project 42-354/2013(SR) UGC-MRP. The authors would like to thank the referee for comments which helped in improving the quality of the paper.

References

- [1] GADEM N.N., KADU A.V., PADOLE P.R., BODADE A.B., CHAUDHARI G.N., *Sens. Trans.*, 110 (2011), 86.
- [2] GOLDMAN A., *Modern Ferrite Technology*, Springer, New York, 1990.
- [3] TATARCHUK T., BOUOUDINA M., VIJAYA J., KENNEDY J.L., *Spinel Ferrite Nanoparticles: Synthesis, Crystal Structure, Properties, and Perspective Applications*, in: FESENKO O., YATSENKO L. (Eds.) *Nanophysics, Nanomaterials, Interface Studies, and Applications*, Springer, Cham, Switzerland 2017, p.305.
- [4] EL HITI M., *Phase Transit.*, 54 (1995), 117.
- [5] LAKSHMAN A., RAO S.V.P., RAO P.B., RAO K.H., *J. Phys. D Appl. Phys.*, 38 (2005), 673.
- [6] RAVINDRE D., REDDY V.B.P., *J. Magn. Magn. Mater.*, 263 (2003), 127.
- [7] THANT A.A., SRIMALA S., CAUNG P., *J. Aust. Ceram. Soc.*, 46 (2010), 11.
- [8] SALMI S., EL AZHARI M., EL GRINI A., HOURMATALLAH A., BENZAKOUR N., BOUSLYKHANE K., MARZOUK A., *IOP Conf. Ser. Mater. Sci. Eng.*, 186 (2017), 1.
- [9] IQBAL M.J., AHMAD Z., MEYDAN T., NLEBEDIM I.C., *Mater. Res. Bull.*, 47 (2012), 344.
- [10] MCCUSKER L.B., DREELE VON R.B., COX D.E., LOUËR D., SCARDI P., *J. Appl. Crystallogr.*, 32 (1999), 36.
- [11] HENDERSON M.B., CHARNOCK J.M., PLANT D.A., *J. Phys.-Condens. Mat.*, 19 (2007), 076214.
- [12] AIRIMIOAEI M., PALAMARU M.N., IORDAN A.R., BERTHET P., DECORSE C., CURECHERIU L., MITOSERIU L., *J. Am. Ceram. Soc.*, 97 (2014), 519.
- [13] HAQUE M.M., MARIA K.H., CHOUDHURY S., BHUIYAN M.A., HAKIM M.A., *JCPR*, 14 (2013) 82.
- [14] BURGER M.J., *J. Crystal-structure Analysis*, John Wiley, New York, 1960.
- [15] PATANGE S.M., SHIRSATH S.E, TOKSHA B.G, JADHAV S.S., SHUKLA S.J, JADHAV K.M., *Appl. Phys. A-Mater.*, 95 (2009), 429.
- [16] KUMAR E.R., KAMZIN A.S., PRAKASH T., *J. Magn. Magn. Mater.*, 378 (2015), 389.
- [17] BERCHMANS L.J., SELVAN R.K., KUMAR P.N.S., AUGUSTIN C.O, *J. Magn. Magn. Mater.*, 279 (2004), 103.
- [18] WALDRON R.D., *Phys. Rev.*, 99 (1955), 1727.

- [19] FRANCO A.JR., SILVA M.S., *J. Appl. Phys.*, 109 (2011), 07B505.
- [20] LOGANATHAN A., KUMAR K., *IJCR*, 7 (2015), 20585.
- [21] UITERT VAN L.G., *J. Chem. Phys.*, 23 (1955), 1883.
- [22] BHAVIKATTIA A.M., MALLIKARJUN M., *IJSR.*, 12 (2015), 232.
- [23] EL HITI M.A., *J. Phys. D Appl. Phys.*, 29 (1996), 501.
- [24] EL-SAYED A.M., *Mater. Chem. Phys.*, 82 (2003), 583.
- [25] METHASIRI T., YOODEE K., TANG I.M., *Physica B*, 101 (1980), 243.
- [26] RAMARAO K., RAJESH BABU B., KISHORE BABU B., VEERAI AH V., RAMARAO S.D., RAJASEKHAR K., VENKATESWARA RAO A., *Physica B*, 528 (2018), 18.
- [27] RAMARAO K., RAJESH BABU B., KISHORE BABU B., VEERAI AH V., RAMARAO S.D., RAJASEKHAR K., VENKATESWARA RAO A., *J. Electron. Mater.*, 47 (2018), 2997.

Received 2017-09-07

Accepted 2018-05-12